

A Deep Joint Source-Channel Coding Scheme for Hybrid Mobile Multi-hop Networks

Chenghong Bian, Yulin Shao, Deniz Gündüz

Abstract—Efficient data transmission across mobile multi-hop networks that connect edge devices to core servers presents significant challenges, particularly due to the variability in link qualities between wireless and wired segments. This variability necessitates a robust transmission scheme that transcends the limitations of existing deep joint source-channel coding (DeepJSCC) strategies, which often struggle at the intersection of analog and digital methods. Addressing this need, this paper introduces a novel hybrid DeepJSCC framework, h-DJSCC, tailored for effective image transmission from edge devices through a network architecture that includes initial wireless transmission followed by multiple wired hops. Our approach harnesses the strengths of DeepJSCC for the initial, variable-quality wireless link to avoid the cliff effect inherent in purely digital schemes. For the subsequent wired hops, which feature more stable and high-capacity connections, we implement digital compression and forwarding techniques to prevent noise accumulation. This dual-mode strategy is adaptable even in scenarios with limited knowledge of the image distribution, enhancing the framework's robustness and utility. Extensive numerical simulations demonstrate that our hybrid solution outperforms traditional fully digital approaches by effectively managing transitions between different network segments and optimizing for variable signal-to-noise ratios (SNRs). We also introduce a fully adaptive h-DJSCC architecture capable of adjusting to different network conditions and achieving diverse rate-distortion objectives, thereby reducing the memory requirements on network nodes.

Index Terms—Mobile edge networks, multi-hop networks, DeepJSCC, variable rate compression, oblivious relay.

I. INTRODUCTION

Multi-hop relay networks are essential for enhancing the coverage of wireless communication systems, enabling seamless connectivity across widely dispersed areas. These networks support the transmission of messages through a sequence of relay nodes, substantially increasing the reach and reliability of wireless communications by overcoming the limitations imposed by physical distance and challenging terrains. In the prevalent configuration of mobile networks, a distinctive hybrid architecture emerges: the data transmission commences at the mobile edge, where devices initially connect via a variable-quality wireless link to a nearby access point. Subsequently, the data journey continues through multiple wired hops until it reaches the core network server, as illustrated in Fig. 1. These subsequent wired links, usually subject to fixed rate constraints, provide stable and high-capacity connections that are pivotal for efficient data management and transmission.

The authors are with the Department of Electrical and Electronic Engineering, Imperial College London, London SW7 2AZ, U.K. (e-mail: {c.bian22, y.shao, d.gunduz}@imperial.ac.uk) This paper will be presented in part at the IEEE International Conference on Communications 2024 [1].

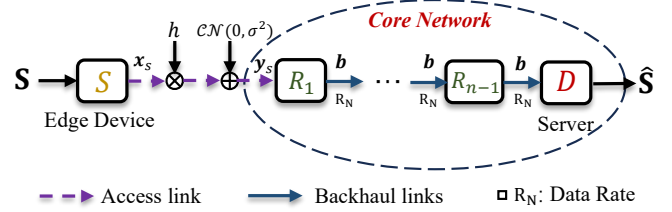


Fig. 1: Schematic of the hybrid multi-hop network architecture. An edge device S transmits data to an edge server D through a series of relay nodes, R_1, \dots, R_{n-1} within the mobile core network. h denotes the fading coefficient.

This paper focuses on the adaption of joint source channel coding (JSCC) in such a hybrid mobile multi-hop network, bringing it one step closer to adoption in realistic network scenarios. Recent advancements have seen deep learning (DL) making significant strides in designing JSCC schemes suitable for wireless channels. Originally proposed in [2], the DeepJSCC methodology has been recognized for its ability to surpass traditional digital communication benchmarks that combine state-of-the-art image compression techniques with near-optimal channel codes. Moreover, it achieves a graceful performance degradation in scenarios of deteriorating channel conditions. In [3]–[6], the DeepJSCC framework is extended to video, speech and point cloud sources, highlighting it as an effective tool for a large variety of applications. More recently, DeepJSCC techniques have also been extended to multi-user scenarios, where [7]–[11] show the superior performance of the DeepJSCC in the three node cooperative relay, the multiple access, and broadcast channels, respectively. This paper aims to explore the potential of DeepJSCC in optimizing data transmission from edge devices through a hybrid network of wireless and wired links, ensuring robust and efficient data delivery to edge servers. The most related works are [12], [13] where the authors investigate DeepJSCC over multi-hop networks. In particular, [12] introduces a term named semantic similarity and optimizes the neural networks to preserve the similarity over the hops, whereas [13] proposes a recursive training methodology to mitigate the noise accumulation problem. Though some performance improvements are attained compared with the naively trained scheme, [12], [13] fail to fit into the considered scenario with wired links.

A key factor underpinning the success of DeepJSCC is its reliance on discrete-time analog transmission (DTAT) [14], which introduces a greater degree of flexibility for channel symbols and ensures that the reception quality at the

receiver is closely tied to fluctuations in channel quality. This refined strategy is in sharp contrast to conventional digital transmission methods, which are characterized by a binary outcome: successful decoding or complete data loss, the latter leads to a precipitous performance drop-off known as the *cliff effect*. However, while the DTAT approach offers distinct advantages in scenarios involving direct, single-hop transmissions, it poses significant challenges within the context of networks involving multiple transmission mediums. In this architecture, data transmitted from the mobile edge to the access point via wireless links and then relayed through a wired network to the edge server, introduces a complex interplay between different transmission characteristics. The initial wireless link, susceptible to channel impairments such as fading and noise, and the subsequent wired hops with fixed rate constraints, require careful management to maintain signal integrity. Here, the signal distortion introduced in the wireless segment and potential bottlenecks in wired segments can lead to a degradation of signal quality – a problem less pronounced in digital systems where data can be regenerated at each node. Consequently, the performance of DeepJSCC tends to decline as the network complexity increases, calling for innovative solutions tailored for hybrid multi-hop network architectures.

In this paper, we introduce a novel DeepJSCC framework, h-DJSCC, tailored for efficient image transmission across the hybrid mobile multi-hop network. The cornerstone of h-DJSCC is the strategic use of DeepJSCC for the first hop (i.e., the access link), capitalizing on its ability to offer variable quality transmission. This choice effectively sidesteps the notorious cliff effect associated with digital schemes, ensuring a more resilient transmission. For the subsequent hops, which are relayed through a wired network with fixed rate constraints, h-DJSCC transitions to a digital transmission mode. This dual-phase approach marries the best of both worlds: it leverages the adaptability of DeepJSCC to mitigate variances in initial channel conditions while employing digital transmission in the later stages to overcome bandwidth limitations and ensure consistent, error-free data transmission. This strategy offers a nuanced balance, providing a robust solution for high-quality image transmission over complex multi-hop networks that involve both wireless and wired segments.

Our main contributions are summarized as follows.

- We introduce h-DJSCC, a novel DeepJSCC framework designed for multi-hop image transmission from mobile edge devices to the core network. This approach leverages a hybrid communication strategy that begins with an analog-based DeepJSCC scheme for the initial wireless link under fluctuating channel conditions, followed by digital coding and modulation schemes for the subsequent wired hops with fixed rate constraints. A neural network-based compression module is deployed at the access point to efficiently convert the received analog DeepJSCC codeword into a digital bit sequence, facilitating flexible trade-offs between transmission latency and reconstruction quality to accommodate diverse network demands.
- We explore the adaptability of the h-DJSCC framework to scenarios where the access point performs oblivious relaying – processing signals based only on past received

signals without knowledge of the transmitted image distribution. This aspect underscores the robustness of the h-DJSCC framework, showing notable performance improvements over traditional methods where relays directly quantize the received signals into bit sequences.

- To tackle practical communication challenges, we propose a fully adaptive h-DJSCC scheme suitable for scenarios where the initial wireless link experiences fluctuating conditions. This scheme is robust across both Additive White Gaussian Noise (AWGN) and Rayleigh fading channels, demonstrating the model's capacity to adjust to various signal-to-noise ratio (SNR) levels and achieve multiple rate-distortion (R-D) points. The fully adaptive h-DJSCC scheme is carefully initialized to avoid succumbing to sub-optimal solutions.
- Through comprehensive numerical experiments, we validate the h-DJSCC framework's superiority over traditional fully digital approaches across different channel conditions and datasets. Our results underscore the fully adaptive h-DJSCC framework's enhanced R-D performance, confirming its practical effectiveness and adaptability to diverse transmission scenarios.

Notations: Throughout the paper, scalars are denoted by normal-face letters (e.g., x), while random variables are denoted by uppercase letters (e.g., X). Matrices and vectors are denoted by bold upper and lower case letters (e.g., \mathbf{X} and \mathbf{x}), respectively. A set is denoted by \mathbb{S} . Transpose and conjugate operators are denoted by $(\cdot)^\top$ and $(\cdot)^*$, respectively.

II. PROBLEM FORMULATION

A. System Model

We consider a multi-hop network, where a mobile edge user S aims to deliver an image to a destination node D with the aid of $(n-1)$ relay nodes $\{R_1, \dots, R_{n-1}\}$ residing in the core network, as depicted in Fig. 1. The backhaul links within the core network are more reliable than the access link between S and R_1 . In particular, we assume the backhaul links are able to deliver information errorlessly and each link is associated with an achievable rate, R_i . Without loss of generalizability, we assume all the nodes are of the same quality, with achievable rates $R_1 = \dots = R_n = R_N$. As illustrated in Fig. 1, the transmission over the backhaul links within the core network can be abstracted as a single hop with an achievable rate R_N .¹ Initially, we base our analysis on the premise that the wireless channel in the first hop operates as AWGN channel. This assumption lays the groundwork for our foundational model, which we will subsequently extend to encompass Rayleigh fading channels in the later sections.

The edge user S encodes image $\mathbf{S} \in \mathbb{R}^{C \times H \times W}$ to channel input vector $\mathbf{x}_s \in \mathbb{C}^k$ using an encoding function² $f_s(\cdot) : \mathbb{R}^{C \times H \times W} \rightarrow \mathbb{C}^k$, where C, H, W denote the number of color

¹This is valid for full-duplex relays. The achievable rate reduces to $\frac{R_N}{n}$ if half-duplex relays are considered.

²We note that k refers to the expected number of channel uses if variable length source encoder is adopted.

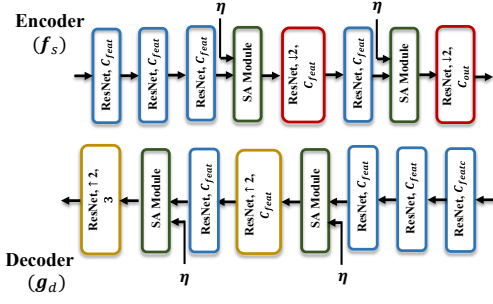


Fig. 2: Neural network architecture for the proposed Deep-JSCC encoder $f_s(\cdot)$ and decoder $g_d(\cdot)$ with SNR-adaptive module.

channels, the height and the width of the image, respectively. The channel input is subject to a power constraint:

$$\frac{1}{k} \|\mathbf{x}_s\|^2 \leq 1. \quad (1)$$

The signal received at the first relay node R_1 (i.e., the access point of the core network) can be expressed as

$$\mathbf{y}_1 = \mathbf{x}_s + \mathbf{w}_s, \quad (2)$$

where $\mathbf{w}_s \sim \mathcal{CN}(0, \sigma^2 \mathbf{I}_k)$. The SNR of the first hop is defined as $\eta \triangleq \frac{1}{\sigma^2}$.

Within the core network, the relays can adopt different processing strategies, such as the fully digital scheme, the naive quantization scheme, and the proposed h-DJSCC scheme detailed later. Different strategies correspond to different processing at the first relay, R_1 , which is denoted by $f_{R_1}(\cdot)$. The output of R_1 is a bit sequence:

$$\mathbf{b}_1 = f_{R_1}(\mathbf{y}_1), \quad (3)$$

where \mathbf{b}_1 is of length k which will be further transmitted over the core network.

Upon receiving \mathbf{b}_1 , the destination reconstructs the original image by a decoding function $f_D(\cdot)$ as $\hat{\mathbf{S}} = f_D(\mathbf{b}_1)$. To evaluate the reconstruction performance of different processing strategies (specified by f_s , f_{R_1} and f_D), the peak signal-to-noise ratio (PSNR) and the structural similarity index (SSIM) are adopted, the PSNR is defined as:

$$\text{PSNR} = 10 \log_{10} \frac{255^2}{\frac{1}{M} \|\mathbf{S} - \hat{\mathbf{S}}\|_F^2}, \quad (4)$$

where $M = CHW$ denotes the total number of pixels in the image \mathbf{S} . The SSIM is defined as:

$$\text{SSIM} = \frac{(2\mu_s\mu_{\hat{s}} + c_1)(2\sigma_{s\hat{s}} + c_2)}{(\mu_s^2 + \mu_{\hat{s}}^2 + c_1)(\sigma_s^2 + \sigma_{\hat{s}}^2 + c_2)}, \quad (5)$$

where $\mu_s, \sigma_s, \sigma_{s\hat{s}}$ are the mean and variance of \mathbf{S} , and the covariance between \mathbf{S} and $\hat{\mathbf{S}}$, respectively. c_1 and c_2 are constants for numeric stability.

B. Existing Methods

We first review existing methods for communication over multi-hop wireless networks, namely, the fully digital transmission and the naive quantization approach.

1) *Fully digital transmission*: The encoder at S first compresses the input image into a bit sequence, denoted by \mathbf{b}_s , which is then channel coded and modulated to form the channel codeword \mathbf{x}_s . We consider the state-of-the-art source encoders (e.g., BPG) which output variable-length codewords, thus, the number of complex channel uses k refers to the expected length of \mathbf{x}_s . The processing operation $f_{R_1}(\cdot)$ at the first relay is simply a channel decoder, denoted as $D_1(\cdot)$, which decodes the received signal, \mathbf{y}_1 to a bit sequence, $\hat{\mathbf{b}}_s$. The bit sequence will be transmitted over the core network and the destination node reconstructs the image using $\hat{\mathbf{b}}_s$.

To better illustrate the processing of the fully digital transmission scheme, we provide a concrete example where the number of channel uses, $k = 768$ and $\eta = 2$ dB which corresponds to the channel capacity $C_s = 1.37$. We adopt a coded modulation scheme with a rate below C_s (for reliable transmission). To be precise, we consider a rate-1/2 LDPC code with 4QAM corresponding to an achievable rate $R_s = 1$ for the first hop. It has been shown by simulations that the coded modulation schemes along with the corresponding belief propagation (BP) decoders are capable to achieve almost zero block error rate (BLER) in the considered scenario. The average number of bits, i.e., $\#\hat{\mathbf{b}}_s$, to be transmitted over the core network is 768 and is delivered to the destination losslessly.

A key weakness of the fully digital transmission is that, the link quality between the source and the first relay node might change over time, and the system suffers from the cliff and leveling effects.

2) *Naive Quantization*: To avoid the cliff and leveling effects, we adopt DeepJSCC for the first hop with analogy transmission where \mathbf{x}_s is a DeepJSCC codeword. The first relay node transforms its received noisy codeword, \mathbf{y}_1 to a bit sequence, \mathbf{b}_1 , and transmits it over the core network. This is analogous to the CPRI compression [15], [16] in the literature where baseband signals are quantized into bits to be transmitted over the fiber. In this paper, we consider a vector quantization approach. In particular, the received signal \mathbf{y}_1 is first partitioned into k/N_v blocks where $N_v \geq 1$ denotes the number of elements in the block. $N_v b$ number of bits is used to quantize each block and the codebook to quantize each block is obtained via Lloyd algorithm which is available at the first relay, R_1 and the destination.

Note that the elements within \mathbf{y}_1 are not identically and independently distributed (i.i.d.). Moreover, the underlying distribution is hard to model, thus, the vector quantization scheme is sub-optimal calling for more advanced compression algorithm which will be detailed in the next section.

III. THE PROPOSED H-DJSCC FRAMEWORK

A. Hybrid Solution

We consider a hybrid scheme (see Fig. 3), where the mobile user adopts DeepJSCC protocol in the first hop to avoid the cliff and leveling effects, whereas the first relay node, R_1 , uses a DNN to compress its received signal, \mathbf{y}_1 to a bit sequence \mathbf{b}_1 which is transmitted over the $(n - 1)$ hops in the core network errorlessly. Then, the decoder at D, takes \mathbf{b}_1 as input

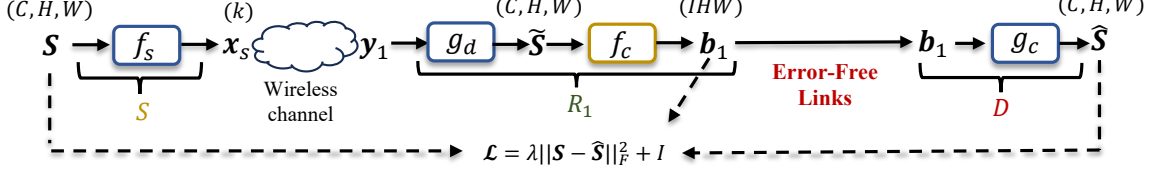


Fig. 3: Illustration of the proposed h-DJSCC framework, where $f_s(\cdot)$ denotes the DeepJSCC encoder at the source node, $g_d(\cdot)$ denotes the DeepJSCC decoder located at R_1 . $f_c(\cdot)$ and $g_c(\cdot)$ represent the compression and decompression modules. The bit output, b_1 of the compression module, $f_c(\cdot)$ is delivered to the destination via error-free links in the core network. We show the dimensions on top of the tensors and vectors for clarity. The loss function, \mathcal{L} , is a summation of the weighted distortion and the bpp (I) defined in (12) used to compress the image \tilde{S} .

to generate the final reconstruction, \hat{S} . The flowchart of the proposed h-DJSCC framework is detailed as follows.

1) *Encoder at S*: The encoder function $f_s(\cdot)$ at S is shown in Fig. 2 which is comprised of 2d CNN layers with residual connection.

2) *Processing at R_1* : A naive solution is to directly quantize the elements of the received signal y_1 to a bit sequence which is illustrated in Section II-B2. However, naively quantizing the received signal leads to a sub-optimal solution, which motivates the employment of a neural compression model.

Instead of directly compressing y_1 , we found it is more beneficial to first transform y_1 into a tensor with the same dimension of the original image S , denoted by \tilde{S} , via a DeepJSCC decoder, $g_d(\cdot)$, whose neural network architecture is shown in Fig. 2, and then apply the neural image compression algorithm [17], denoted as $f_c(\cdot)$, to compress \tilde{S} into a bit sequence b_1 . The processing of the neural compression model is summarized as follows (see also Fig. 4): After obtaining the reconstructed image \tilde{S} , we first use non-linear transformation blocks, denoted by $g_a(\cdot)$, which is comprised of 2D CNNs with C_z output channels to generate a latent tensor $z \in \mathbb{R}^{C_z \times H/4 \times W/4}$, which is fed to the hyper-latent encoder, $h_a(\cdot)$, to generate the hyper-latent $v \in \mathbb{R}^{C_v \times H/16 \times W/16}$.

$$z = g_a(\tilde{S}); \quad v = h_a(z). \quad (6)$$

The hyper-latent v is introduced with the aim to remove the dependency between the elements in z , such that given v , the probability density function (pdf) of z will be the product of the pdf's of its elements.

It is worth mentioning that the neural image compression model involves two phases, the training and deployment phases. In the deployment phase, we round each element of the two latent vectors, z_i and v_i , to the nearest integers, \hat{z}_i and \hat{v}_i :

$$\hat{z}_i, \hat{v}_i = Q(z_i), Q(v_i), \quad (7)$$

where $Q(\cdot)$ denotes the quantization operation. We then arithmetically encode the quantized vectors according to their own probability distributions. In the training phase, however, the rounding operation is infeasible as its gradient is one only at integer points, and zero otherwise. Thus, during training, we use \tilde{z}, \tilde{v} to replace the quantized vectors \hat{z}, \hat{v} , where the elements \tilde{z}_i, \tilde{v}_i are obtained by adding uniform noise, $\mathcal{U}(-\frac{1}{2}, \frac{1}{2})$ (to model the quantization noise) to z_i, v_i . A hyper

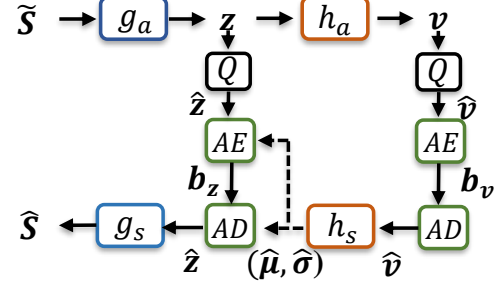


Fig. 4: Illustration of the compression and decompression modules, $f_c(\cdot)$ and $g_c(\cdot)$, respectively. In particular, $g_a(\cdot), h_a(\cdot)$ are the non-linear transform blocks to generate the latent vectors z, v , whereas $g_s(\cdot), h_s(\cdot)$ are adopted to facilitate the synthesis of \hat{S}, \hat{z} . The predicted tensors $\hat{\mu}, \hat{\sigma}$ are used for the arithmetic encoding and decoding of \hat{z} and b_z .

latent decoder, $h_s(\cdot)$, with two upsampling layers takes \tilde{v} as input, and outputs two tensors³ $\tilde{\mu}$ and $\tilde{\sigma}$ with the same dimension as \tilde{z} . Then, we model the pdf of \tilde{z} as:

$$p(\tilde{z}|\tilde{v}) = \prod_i \left(\mathcal{N}(\tilde{\mu}_i, \tilde{\sigma}_i^2) * \mathcal{U}(-\frac{1}{2}, \frac{1}{2}) \right) (\tilde{z}_i), \quad (8)$$

$$\tilde{\mu}, \tilde{\sigma} = h_s(\tilde{v}, \theta),$$

where θ denotes the parameters for $h_s(\cdot)$ and $*$ represents convolution. For the hyper latent \tilde{v} , we consider modeling it also using a fully factorized model as:

$$p(\tilde{v}|\phi) = \prod_i \left(p_{\tilde{v}_i|\phi_i}(\phi_i) * \mathcal{U}(-\frac{1}{2}, \frac{1}{2}) \right) (\tilde{v}_i), \quad (9)$$

where ϕ denotes a collection of parameters to parameterize the univariate distribution.

Once the models are trained and deployed, the latent and hyper-latent vectors z, v can be obtained from the reconstructed image \tilde{S} . We use an arithmetic encoder to encode the rounded \hat{z}, \hat{v} to the bit sequence $b_1 = (b_z, b_v)$ according to the optimized pdfs in (8) and (9) by simply replacing \tilde{z}, \tilde{v} by \hat{z}, \hat{v} . The bit sequence will be forwarded to the destination via the subsequent links. Due to the fact that different images

³Note that the $\tilde{\sigma}$ here is different from the σ^2 in (2) which represents the power of the channel noise.

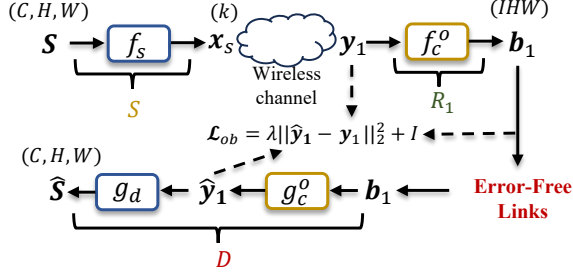


Fig. 5: The framework of the oblivious relaying where R_1 only has access to the past received signal y_1 .

contain different amount of information, the length of the bit sequence varies, and, similarly to the fully digital transmission, we evaluate the expected amount of latency as

$$k' = \frac{1}{R_N} \mathbb{E}_{\tilde{S} \sim p_{\tilde{S}}} (\#b_1), \quad (10)$$

where $\#b_1$ denotes the number of bits in the sequence while R_N is the achievable rate of the core network.

3) *Neural processing at D*: The destination node retrieves the bit sequence b_1 correctly, and employs an arithmetic decoder (AD) to first generate the rounded latent vector \hat{v} , which is then fed to $h_s(\cdot)$ to obtain $\hat{\mu}, \hat{\sigma}$. Then, another AD takes the mean and variance, $\hat{\mu}, \hat{\sigma}$ along with the sequence b_z to produce the rounded latent vector \hat{z} . Finally, the decompressor, $g_c(\cdot)$ takes \hat{z} as input and outputs \hat{S} .

Loss function for the h-DJSCC framework. Similarly to the general source compression problem, there is a trade-off between the amount of bits used to compress y_1 (or equivalently, \tilde{S}) and the reconstruction performance at D. To achieve different trade-off points in the rate-distortion plane, we introduce a variable λ and the loss function is written as:

$$\mathcal{L} = \lambda \|S - \hat{S}\|_F^2 + I, \quad (11)$$

where $I = I_z + I_v$ is the summation of the bit per pixel (bpp) for compressing \tilde{z} and \tilde{v} , which is defined by the number of bits divided by the height H and width W of the image. Note that the notation \tilde{z}, \tilde{v} indicate the training phase⁴ and the rate can be further expressed as:

$$I = \frac{1}{HW} \mathbb{E}_{\tilde{z}, \tilde{v} \sim q} [-\log_2(p_{\tilde{z}|\tilde{v}}(\tilde{z}|\tilde{v})) - \log_2(p_{\tilde{v}}(\tilde{v}))], \quad (12)$$

where the first and second terms represent I_z and I_v , respectively, while q denotes the posterior of \tilde{z}, \tilde{v} given reconstructed image \tilde{S} at R_1 , which follows a uniform distribution centered at $g_a(\cdot)$ and $h_a(\cdot)$ output, z and v :

$$q(\tilde{z}, \tilde{v}|\tilde{S}) = \prod_i \mathcal{U}(\tilde{z}_i | z_i - \frac{1}{2}, z_i + \frac{1}{2}) \mathcal{U}(\tilde{v}_i | v_i - \frac{1}{2}, v_i + \frac{1}{2}). \quad (13)$$

⁴Definition of I is the same for the deployment phase obtained by replacing \tilde{z} and \tilde{v} with \hat{z} and \hat{v} .

B. Oblivious Relaying

As shown in Fig. 3, the first relay R_1 utilizes the DeepJSCC decoder $g_d(\cdot)$ which is jointly optimized with $f_s(\cdot)$, $f_c(\cdot)$ and $g_c(\cdot)$ to achieve the best reconstruction performance at the destination. This implies that the relay has access to the distribution of the transmitted image and the neural processing function, $f_s(\cdot)$ at the source. However, in some scenarios, the relay is unaware of the exact processing at the source as well as the underlying data distribution⁵, P_S , which motivates a different relaying protocol known as oblivious relaying [18], [19] in the literature. In particular, the authors in [18] consider a scenario where the relay maps its received signal to a codeword from a randomly generated codebook which will be forwarded to the destination.

In our case, instead of using a randomly generated codebook, the relay compresses y_1 using a DNN. As shown in Fig. 5, the compressor, $f_c^o(\cdot)$ is employed at R_1 to compress the received signal into bits and the decompressor, $g_c^o(\cdot)$, located at the destination, reconstructs the received signal as:

$$\hat{y}_1 = g_c^o(f_c^o(y_1)). \quad (14)$$

Since in the considered oblivious relaying setup, the relay only has access to y_1 , the loss function is expressed as:

$$\mathcal{L}_{ob} = \lambda \|y_1 - \hat{y}_1\|_2^2 + I, \quad (15)$$

where I is defined in (12). Finally, the DeepJSCC decoder, $g_d(\cdot)$ at the destination takes \hat{y}_1 as input and outputs the reconstructed image \hat{S} .

IV. ADAPTIVE H-DJSCC TRANSMISSION

In the previous section, for a given η value, different models are trained to achieve different points on the R-D trade-off by choosing different λ values from a pre-defined set, denoted as Λ . Since the channel quality between S and R_1 is assumed to change over time, $|\Lambda||H|$ different models would be required⁶ to achieve satisfactory R-D performance causing severe storage problem. Thus, we would like to develop a fully adaptive h-DJSCC framework that is robust to variations in η values and capable of achieving different points on the R-D curve.

In this section, we introduce the neural network architecture and the corresponding training procedure for the proposed fully adaptive h-DJSCC framework.

A. SNR-adaptive DeepJSCC

By incorporating the SA module, a single DeepJSCC model can achieve the best reconstruction performance achievable by separately trained models at a range of SNRs. The intuition is that, for different η values, the DeepJSCC encoder with SA module judiciously decides which features to convey to the receiver, and at what fidelity. To be precise, we denote the input feature to the SA module as $Z_l \in \mathbb{R}^{C_l \times H_l \times W_l}$, where

⁵It might be the case where the source and the destination wish to convey some private message S which should not be decoded by the relays.

⁶Here we consider the variable η is chosen from a discrete set H with $|H|$ elements. The proposed fully adaptive h-DJSCC framework can adapt to continuous η values.

C_l, H_l, W_l refer to the number of channels, the height and the width of the feature, respectively. Then, the weight $\mathbf{w} \in \mathbb{R}^{C_l}$ is calculated according to \mathbf{Z}_l and η and is further multiplied with the input feature in a channel-wise manner to obtain the output $\mathbf{Z}_{l,SA} \in \mathbb{R}^{C_l \times H_l \times W_l}$:

$$\mathbf{w} = \text{MLP}\left(\left[\frac{1}{H_l W_l} \sum_{i,j} \mathbf{Z}_l[:, i, j], \eta\right]\right),$$

$$\mathbf{Z}_{l,SA}[k] = w_k \mathbf{Z}_l[k], \quad k \in [1, C_l], \quad (16)$$

where MLP denotes the Multi-Layer Perceptron layer. Note that different channels of \mathbf{Z}_l may contain different features and different levels of protection against channel noise. By multiplying the SNR-aware weight, \mathbf{w} , with \mathbf{Z}_l , a different balance between the information content of the conveyed features and the level of robustness is achieved for different η values. Despite of its impressive performance, there is no quantitative verification of the concepts such as the information content and the levels of protection which we aim to show it from a R-D perspective.

To be specific, we consider an SNR-adaptive DeepJSCC encoder, $f_s(\cdot, \eta)$ which produces different transmitted signals, \mathbf{x}_η for different input images and SNR values:

$$\mathbf{x}_\eta = f_s(\mathbf{S}, \eta). \quad (17)$$

The SNR-adaptive DeepJSCC decoder, $g_d(\cdot, \eta)$ produces the reconstructed image as:

$$\mathbf{S}_\eta = g_d(\mathbf{x}_\eta, \eta). \quad (18)$$

Then, we compress \mathbf{S}_η to bits and decompress the bit sequence to obtain $\hat{\mathbf{S}}_\eta$, which is of the same dimension as \mathbf{S}_η . Different models corresponding to different λ values are trained where the loss function is expressed as:

$$\mathcal{L}_{SA} = \lambda \|\hat{\mathbf{S}}_\eta - \mathbf{S}_\eta\|_2^2 + I, \quad (19)$$

where I is defined in (12). We set $\lambda \in \{200, 400, 800, 1600, 3200\}$ and $\eta \in \{1, 5, 9\}$ dB for this simulation. As shown in Fig. 6, when η is high, e.g., 9 dB, the output of the SNR-adaptive DeepJSCC encoder, \mathbf{x}_η , contains a larger proportion of information content leading to an inferior R-D curve. On the other hand, when $\eta = 1$ dB, the best R-D curve is obtained showing a large amount of redundancy is produced to protect the information content which aligns with the analysis in [20].

B. SNR-adaptive h-DJSCC framework

We then focus on the SNR-adaptive neural compression model located at R_1 , whose input is the reconstructed image $\hat{\mathbf{S}}_\eta$. Note that the reconstructed images corresponding to different η values follow different distributions, $P_{\hat{\mathbf{S}}_\eta}$. As analyzed in the previous subsection, $\hat{\mathbf{S}}_\eta$ corresponding to different η values contain different amount of information content. Thus, the SNR-adaptive compression model takes η as an additional input compared to the compression model in Section III.

We parameterize the analysis transformations, $g_a(\cdot, \eta)$ and $h_a(\cdot, \eta)$, as well as the synthesis transformations, $g_s(\cdot, \eta)$ and $h_s(\cdot, \eta)$ of the SNR-adaptive compression and decompression

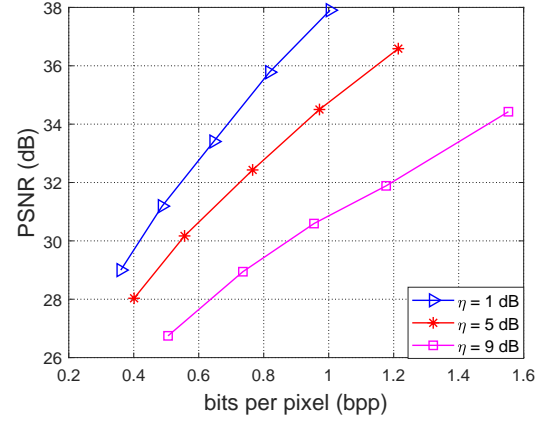


Fig. 6: The R-D performance achieved by compressing the output of the SNR-adaptive DeepJSCC encoder for different η values.

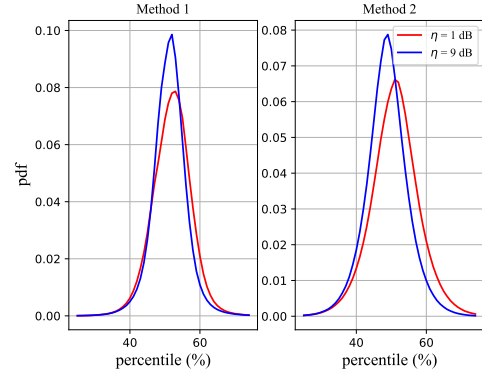


Fig. 7: The comparison of the empirical distribution, $\hat{P}_{\hat{\mathbf{x}}_\eta}$, obtained by the h-DJSCC models that is randomly initialized (left) and initialized using a pre-trained SNR-adaptive DeepJSCC model (right). The empirical distributions are evaluated under two different $\eta = \{1, 9\}$ dB values.

models by ResNets with SA modules. The latents \mathbf{z}_η and \mathbf{v}_η are obtained as:

$$\mathbf{z}_\eta = g_a(\tilde{\mathbf{S}}_\eta, \eta); \quad \mathbf{v}_\eta = h_a(\mathbf{z}_\eta, \eta). \quad (20)$$

During training, we focus on estimating the bit budget to encode the above latents. In particular, the pdf of $\tilde{\mathbf{v}}_\eta$ is obtained by replacing $\tilde{\mathbf{v}}$ in (9) by $\tilde{\mathbf{v}}_\eta$:

$$p_{\tilde{\mathbf{v}}_\eta|\phi} = \prod_i (p_{\tilde{\mathbf{v}}_\eta|\phi_i}(\phi_i) * \mathcal{U}(-\frac{1}{2}, \frac{1}{2}))(\tilde{\mathbf{v}}_\eta), \quad (21)$$

where $\tilde{\mathbf{v}}_\eta$ is obtained by adding uniform noise to \mathbf{v}_η . Note that in the above equation, we make an assumption that the probability model, $p_{\tilde{\mathbf{v}}_\eta|\phi_i}(\phi_i) * \mathcal{U}(-\frac{1}{2}, \frac{1}{2})$ is capable to provide accurate pdf for the latent variable $\tilde{\mathbf{v}}_\eta$ with varying η values. Similarly, the pdf of \mathbf{z}_η can be expressed by replacing $\tilde{\mathbf{z}}$ and $\tilde{\mathbf{v}}$ in (8) by $\tilde{\mathbf{z}}_\eta$ and $\tilde{\mathbf{v}}_\eta$ which is omitted due to the page limit.

It is worth emphasizing that it is also possible to let the probability model $p_{\tilde{\mathbf{v}}_\eta|\phi}$ be aware of different SNR values by

concatenating the SNR value along with the input tensor, \tilde{v}_η . However, we found by experiments that the neural network $h_a(\cdot, \eta)$ is already capable of encoding the varying SNR values into its output, \tilde{v}_η , leading to satisfactory results, thus we adopt the formula in (21) throughout the paper.

The SNR-adaptive h-DJSCC framework is optimized in an end-to-end fashion. In particular, for each batch, we sample $\eta \sim \mathcal{U}(\eta_{min}, \eta_{max})$, and the loss corresponding to the sampled SNR value is calculated according to (11). It is worth emphasizing that the initialization method plays a vital role in achieving satisfactory R-D performances. We found in our experiments that adopting random initialization for all the neural network weights leads to highly sub-optimal solution.

To understand this phenomena, we explore the distribution of the latent vector, \mathbf{x}_η . Instead of directly studying the complex vector, we convert it to a real-valued one, denoted by $\mathbf{x}'_\eta \in \mathbb{R}^{2k}$ and normalize its elements as:

$$\tilde{\mathbf{x}}_\eta = \frac{\mathbf{x}'_\eta - \min(\mathbf{x}'_\eta)}{\max(\mathbf{x}'_\eta) - \min(\mathbf{x}'_\eta)}. \quad (22)$$

To estimate the empirical distribution, $\hat{P}_{\tilde{\mathbf{x}}_\eta}(\cdot)$, we partition the unit interval to 100 bins, and calculate the number of elements that fall into each bin. $N = 10^4$ realizations of $\tilde{\mathbf{x}}_\eta$ are collected and $\hat{P}_{\tilde{\mathbf{x}}_\eta}(\cdot)$ is obtained by averaging over all $2kN$ elements:

$$\hat{P}_{\tilde{\mathbf{x}}_\eta}(i) = \frac{1}{2kN} \sum_{n=1}^N \sum_{j=1}^{2k} \mathbf{1} \left(\frac{i-1}{100} < \tilde{\mathbf{X}}_\eta[n, j] \leq \frac{i}{100} \right), \quad (23)$$

where $\tilde{\mathbf{X}}_\eta \in \mathbb{R}^{N \times 2k}$ is a matrix obtained by stacking N different realizations and $\mathbf{1}(\cdot)$ is the indicator function.

On the left hand side of Fig. 7, the empirical distribution $\hat{P}_{\tilde{\mathbf{x}}_\eta}$ for the SNR-adaptive h-DJSCC framework with random neural network weight initialization is plotted for $\eta = \{1, 9\}$ dB. It can be seen that the two distributions are quite close to each other. This implies that the scheme converges to a sub-optimal solution as the two distributions need to be more distinct w.r.t different channel qualities. However, it is hard to explicitly design a loss function for the two output distributions corresponding to different SNRs to make them more distinguishable. Fortunately, we find by experiments that the SNR-adaptive DeepJSCC encoder (without being jointly trained with the compression models) produces the desired output distribution. Thus, we initialize the SNR-adaptive h-DJSCC model using the pre-trained SNR-adaptive DeepJSCC model. As will be shown in the simulation section, the above training approach fulfills the SNR-adaptive objective. Moreover, by comparing the right hand side of Fig. 7 with the left, we observe that the pre-trained model yields more ‘distinct’ output distribution w.r.t different SNR values.

C. Fully adaptive h-DJSCC framework

Finally, we introduce the fully adaptive h-DJSCC framework. We will first discuss the variable rate h-DJSCC framework with a fixed η value, inspired by [21]–[23] for image compression. In particular, [21]–[23] mitigate the problem by introducing extra learnable parameters called scaling factors

Algorithm 1: Training procedure of the proposed fully adaptive h-DJSCC framework over a fading channel.

Input : $\{\mathcal{S}\}_{1:N}, \Lambda, \eta_{min}, \eta_{max}, Epochs$
Output: $\hat{\mathcal{S}}_{\ell, \eta}, I_{\ell, \eta}$

- 1 **Initialization:**
- 2 Initialize $f_s(\cdot, \eta), g_d(\cdot, \eta)$ using pre-trained model [20].
- 3 Randomly initialize $\{f_c(\cdot, \eta), g_c(\cdot, \eta)\}$ consists of $\{\mathbf{A}, \mathbf{A}', \mathbf{B}, \mathbf{B}', g_a(\cdot, \eta), g_s(\cdot, \eta), h_a(\cdot, \eta), h_s(\cdot, \eta)\}$
- 4 %% **Training Phase**
- 5 **for** $t = 1$ **to** $Epochs$ **do**
- 6 **for** $b = 1$ **to** \mathcal{B} **do**
- 7 Sample $\lambda_\ell \sim \Lambda, \eta \sim \mathcal{U}(\eta_{min}, \eta_{max})$,
- 8 Sample $h \sim \mathcal{CN}(0, 1)$.
- 9 % **SNR-adaptive DeepJSCC model:**
- 10 **if with CSIT then**
- 11 $\mathbf{x}_\eta = \frac{h^*}{|h|} f_s(\mathcal{S}, |h|^2 \eta)$.
- 12 **else**
- 13 $\mathbf{x}_\eta = f_s(\mathcal{S})$. ▷ Source Node
- 14 $\mathbf{y}_\eta = h\mathbf{x}_\eta + \mathbf{w}$, ▷ Channel
- 15 **if with CSIT then**
- 16 $\hat{\mathbf{x}}_\eta = \frac{|h|\mathbf{y}_\eta}{|h|^2 + 1/\eta}$.
- 17 **else**
- 18 $\hat{\mathbf{x}}_\eta = \frac{h^*\mathbf{y}_\eta}{|h|^2 + 1/\eta}$.
- 19 $\tilde{\mathcal{S}}_\eta = g_d(\hat{\mathbf{x}}_\eta, \eta)$. ▷ First Relay
- 20 % **SNR-adaptive and variable rate compression:**
- 21 $\mathbf{z}_{\ell, \eta} = g_a(\tilde{\mathcal{S}}_\eta, \eta) \otimes \mathbf{a}_\ell$,
- 22 $\mathbf{v}_{\ell, \eta} = h_a(\mathbf{z}_{\ell, \eta}, \eta) \otimes \mathbf{b}_\ell$,
- 23 $\tilde{\mathbf{z}}_{\ell, \eta}, \tilde{\mathbf{v}}_{\ell, \eta} = \mathbf{z}_{\ell, \eta} + \mathcal{U}(-\frac{1}{2}, \frac{1}{2}), \mathbf{v}_{\ell, \eta} + \mathcal{U}(-\frac{1}{2}, \frac{1}{2})$,
- 24 $\tilde{\mathbf{z}}'_{\ell, \eta} = \tilde{\mathbf{z}}_{\ell, \eta} \otimes \mathbf{a}'_\ell$,
- 25 $\hat{\mathcal{S}}_{\ell, \eta} = g_s(\tilde{\mathbf{z}}'_{\ell, \eta}, \eta)$,
- 26 **Estimating entropy:**
- 27 $\tilde{\mathbf{v}}'_{\ell, \eta} = \tilde{\mathbf{v}}_{\ell, \eta} \otimes \mathbf{b}'_\ell$,
- 28 $\tilde{\boldsymbol{\mu}}_{\ell, \eta}, \tilde{\boldsymbol{\sigma}}_{\ell, \eta} = h_s(\tilde{\mathbf{v}}'_{\ell, \eta}, \eta)$,
- 29 $I_{v, \ell, \eta} = -\log_2(p_{\tilde{\mathbf{v}}_{\ell, \eta}})$,
- 30 $I_{z, \ell, \eta} = -\log_2(p_{\tilde{\mathbf{z}}_{\ell, \eta}})$, ▷ $p_{\tilde{\mathbf{v}}_{\ell, \eta}}$ and $p_{\tilde{\mathbf{z}}_{\ell, \eta}}$ are calculated in (27) using $\tilde{\boldsymbol{\mu}}_{\ell, \eta}$ and $\tilde{\boldsymbol{\sigma}}_{\ell, \eta}$.
- 31 $I_{\ell, \eta} = I_{z, \ell, \eta} + I_{v, \ell, \eta}$,
- 32 % **Loss Function:**
- 33 $\mathcal{L}_{fa} = \lambda_\ell \|\mathcal{S} - \hat{\mathcal{S}}_{\ell, \eta}\|_F^2 + I_{\ell, \eta}$,
- 34 Optimize parameters in $f_c(\cdot, \eta)$ and $g_c(\cdot, \eta)$ via gradient descent.

for each point on the R-D curve. The scaling factors for each R-D point scale the latent tensors in a channel-wise manner following the intuition that, different channels of the latent tensors are of different levels of importance, i.e., some channels may contain low-frequency components of the image while the others may be comprised of high-frequency component corresponding to the fine-grained features. When a lower rate is required, the channels containing the low-frequency features should be emphasized. When a higher rate is allowed, we can allocate more bits to represent high-

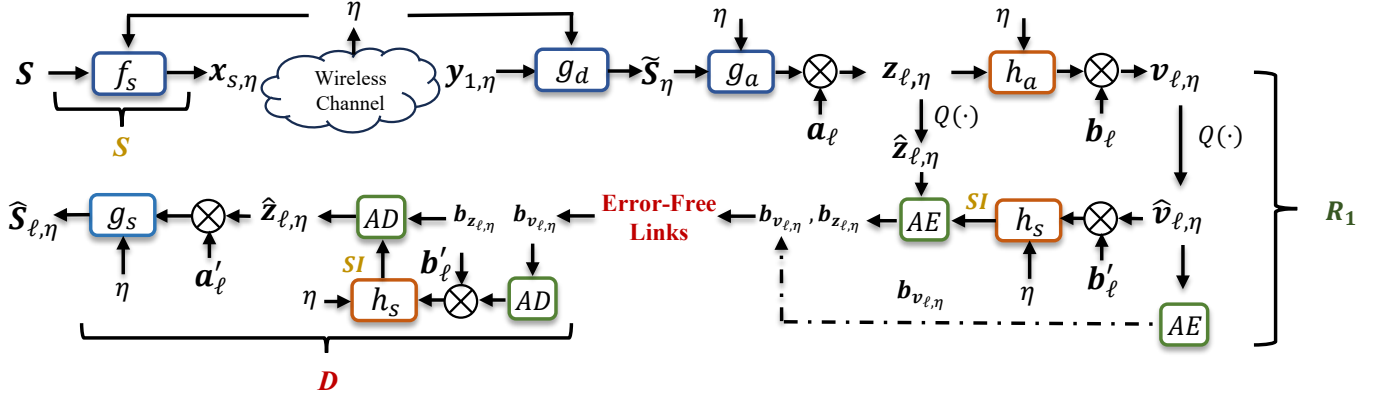


Fig. 8: The flowchart of the proposed fully adaptive h-DJSCC framework. It is applicable to both AWGN and fading channels where η is fed to all the neural network modules, $\{f_s(\cdot, \eta), g_d(\cdot, \eta), g_a(\cdot, \eta), h_a(\cdot, \eta), h_s(\cdot, \eta), g_s(\cdot, \eta)\}$ to achieve the SNR-adaptive objective. The AE and AD denote the arithmetic encoding and decoding blocks, respectively. We consider the R-D performance corresponding to λ_ℓ with the scaling factors $\{a_\ell, a'_\ell, b_\ell, b'_\ell\}$. Finally, SI is used to represent $\mu_{\ell, \eta}$ and $\sigma_{\ell, \eta}^2$.

frequency features.

Following the procedure described in [22], we introduce four sets of weights, namely, $\{A, A', B, B'\} \triangleq \{a_\ell, a'_\ell, b_\ell, b'_\ell\}$, $\ell \in [1, |\Lambda|]$. In particular, $a_\ell = \{a_{\ell,1}, \dots, a_{\ell,C_z}\}$ and $a'_\ell = \{a'_{\ell,1}, \dots, a'_{\ell,C_z}\}$ are employed for the output of the $g_a(\cdot)$ module, z , and the input to the $g_s(\cdot)$ module, \hat{z}_ℓ , respectively⁷. In particular, the scaling and rescaling operations can be expressed as:

$$\begin{aligned} z_\ell &= z \otimes a_\ell, \\ \hat{z}'_\ell &= \hat{z}_\ell \otimes a'_\ell, \end{aligned} \quad (24)$$

where \otimes denotes channel-wise multiplication, \hat{z}_ℓ denotes the quantized version of z_ℓ and \hat{z}'_ℓ is the rescaled tensor which is fed to $g_s(\cdot)$ to generate the reconstructed image. The hyper latents, v and \hat{v}_ℓ also experience the same scaling and rescaling processes using $b_\ell = \{b_{\ell,1}, \dots, b_{\ell,C_v}\}$ and $b'_\ell = \{b'_{\ell,1}, \dots, b'_{\ell,C_v}\}$. The training of the variable rate h-DJSCC framework follows similar procedure as in Section III. We further note that each set of the weights, $\{a_\ell, a'_\ell, b_\ell, b'_\ell\}$ are optimized for a specific λ_ℓ .

To gain more insights into the scaling operations, we point out that for a large bit budget (corresponding to a large λ_ℓ value), the elements in a_ℓ will generally be larger. This can be understood from the quantization process, when a small $a_{\ell,i}$ value is multiplied with the i -th channel, z_i , the elements of the quantized output, $\hat{z}_{\ell,i}$ can only be chosen from a small set of integers resulting in less bits to compress. When a large $a_{\ell,i}$ value is adopted, the candidate set of $\hat{z}_{\ell,i}$ values are larger, leading to a better reconstruction performance. We further note that due to the difference among the channels, in general, the relation that $a_{\ell_1} = c a_{\ell_2}$ does not hold for $\ell_1 \neq \ell_2$, where c is a constant; that is, the weights do not grow linearly with the bit budget.

Finally, we introduce the fully adaptive model where the λ values are chosen from a pre-defined candidate set Λ and η varies within the range $[\eta_{min}, \eta_{max}]$. To prevent the fully adap-

tive h-DJSCC framework from converging to a sub-optimal solution as discussed in Section IV-B, we first train the SNR-adaptive DeepJSCC model with a varying $\eta \in [\eta_{min}, \eta_{max}]$ and use it to initialize the DeepJSCC encoder and decoder, $f_s(\cdot, \eta)$ and $g_d(\cdot, \eta)$ of the fully adaptive h-DJSCC framework. The weights of the compression and decompression modules, $f_c(\cdot, \eta)$ and $g_c(\cdot, \eta)$ of the fully adaptive h-DJSCC framework are initialized randomly.

The flowchart of the fully adaptive h-DJSCC framework is shown in Fig. 8. To start with, the DeepJSCC encoder at the source node S takes η and the image S as input to generate the transmitted signal, $x_{s,\eta}$. After passing the channel, the DeepJSCC decoder at R_1 takes the received signal, $y_{1,\eta}$ and the SNR value to produce the reconstructed image, \hat{S}_η , which will be further processed by the SNR-adaptive variable rate compression module, $f_c(\cdot, \eta)$ to generate z_η and v_η . We multiply the corresponding weights, a_ℓ and b_ℓ , with the latent tensors, z_η and v_η , in a channel-wise manner. The scaled tensors will be quantized and arithmetically encoded into a bit sequence, which is then transmitted over the error free links⁸. At the destination node, D, $\hat{v}_{\ell,\eta}$ is first arithmetically decoded and rescaled using the weight, b'_ℓ . Then, $\hat{z}_{\ell,\eta}$ is arithmetically decoded with $\mu_{\ell,\eta}, \sigma_{\ell,\eta}$ as additional input which are generated using $\hat{v}_{\ell,\eta}$. Finally, we rescale $\hat{z}_{\ell,\eta}$ using a'_ℓ and the decompression module, $g_c(\cdot, \eta)$ takes the rescaled $\hat{z}'_{\ell,\eta}$ as input to generate the reconstructed image, $\hat{S}_{\ell,\eta}$. The overall loss function for the fully adaptive h-DJSCC framework can be expressed as:

$$\mathcal{L}_{fa} = \mathbb{E}_{\lambda_\ell \sim \Lambda, \eta \sim \mathcal{U}(\eta_{min}, \eta_{max})} \lambda_\ell \|S - \hat{S}_{\ell,\eta}\|_F^2 + I_{\ell,\eta}, \quad (25)$$

where $I_{\ell,\eta}$ can be estimated as follows:

$$I_{\ell,\eta} = \frac{1}{HW} \mathbb{E}_{\tilde{z}_{\ell,\eta}, \tilde{v}_{\ell,\eta} \sim q} [-\log_2(p_{\tilde{z}_{\ell,\eta}|\tilde{v}_{\ell,\eta}}(\tilde{z}_{\ell,\eta}|\tilde{v}_{\ell,\eta})) - \log_2(p_{\tilde{v}_{\ell,\eta}}(\tilde{v}_{\ell,\eta}))]. \quad (26)$$

Note that the p terms denote the prior distributions that are

⁷We first ignore the η subscript of the latent vectors z and v for simplicity.

⁸The noise over the hops is assumed to be removed via channel codes.

optimized during training while q terms represent the posterior distribution given $\tilde{\mathbf{S}}_\eta$. We provide the exact forms of the p terms which resemble that in (8) and (9):

$$\begin{aligned} p(\tilde{\mathbf{z}}_{\ell,\eta}|\tilde{\mathbf{v}}_{\ell,\eta}) &= \prod_i (\mathcal{N}(\tilde{\mu}_{\ell,\eta,i}, \tilde{\sigma}_{\ell,\eta,i}^2) * \mathcal{U}(-\frac{1}{2}, \frac{1}{2}))(\tilde{\mathbf{z}}_{\ell,\eta,i}) \\ \tilde{\mu}_{\ell,\eta}, \tilde{\sigma}_{\ell,\eta} &= h_s(\tilde{\mathbf{v}}_{\ell,\eta}, \eta, \theta) \\ p\tilde{\mathbf{v}}_{\ell,\eta}|\phi &= \prod_i (p\tilde{\mathbf{v}}_{\ell,\eta,i}|\phi_i * \mathcal{U}(-\frac{1}{2}, \frac{1}{2}))(\tilde{\mathbf{v}}_{\ell,\eta,i}). \end{aligned} \quad (27)$$

as well as the q term which is similar with that in (13):

$$\begin{aligned} q(\tilde{\mathbf{z}}_{\ell,\eta}, \tilde{\mathbf{v}}_{\ell,\eta}|\tilde{\mathbf{S}}_\eta) &= \prod_i \mathcal{U}(\tilde{\mathbf{z}}_{\ell,\eta,i}|\mathbf{z}_{\ell,\eta,i} - \frac{1}{2}, \mathbf{z}_{\ell,\eta,i} + \frac{1}{2}) \\ &\quad \mathcal{U}(\tilde{\mathbf{v}}_{\ell,\eta,i}|\mathbf{v}_{\ell,\eta,i} - \frac{1}{2}, \mathbf{v}_{\ell,\eta,i} + \frac{1}{2}), \end{aligned} \quad (28)$$

where $\mathbf{z}_{\ell,\eta,i}$ denotes the i -th channel of $\mathbf{z}_{\ell,\eta}$.

D. Fading channel

Finally, we evaluate the fully adaptive h-DJSCC framework over fading channels. To be specific, the link between S and R_1 is replaced by a Rayleigh fading channel while the remaining hops within the core network are kept the same. We first consider the case with a fixed η value.

Two different setups of the Rayleigh fading channel are considered, in the first case, we assume the channel state information (CSI), denoted by h , is available to both S and R_1 . In the second case, however, only the receiver has access to the CSI.

In the first scenario, the source node utilizes the CSI as an additional input to generate its channel input vector, \mathbf{x}_s :

$$\mathbf{x}_s = f_s(\mathbf{S}, |h|^2\eta), \quad (29)$$

where $|h|^2\eta$ is the effective SNR. It then precodes \mathbf{x}_s as:

$$\tilde{\mathbf{x}}_s = \frac{h^*}{|h|} \mathbf{x}_s. \quad (30)$$

The received signal at R_1 can be expressed as:

$$\mathbf{y}_1 = h\tilde{\mathbf{x}}_s + \mathbf{w}_s = |h|\mathbf{x}_s + \mathbf{w}_s, \quad (31)$$

where the fading coefficient, h follows a complex Gaussian distribution, i.e., $h \sim \mathcal{CN}(0, 1)$ and $\mathbf{w}_s \sim \mathcal{CN}(\mathbf{0}, \frac{1}{\eta}\mathbf{I}_k)$. The first relay node receives \mathbf{y}_1 and applies the minimum mean square error (MMSE) equalization to estimate \mathbf{x}_s :

$$\hat{\mathbf{x}}_s = \frac{|h|\mathbf{y}_1}{|h|^2 + 1/\eta}. \quad (32)$$

For the second scenario, the source generates $\mathbf{x}_s = f_s(\mathbf{S}, \eta)$ and directly transmits it to the channel as it has no access to CSI. The MMSE equalization in this case is expressed as:

$$\hat{\mathbf{x}}_s = \frac{h^*\mathbf{y}_1}{|h|^2 + 1/\eta}. \quad (33)$$

For both setups, the output, $\hat{\mathbf{x}}_s$ is fed to the subsequent DeepJSCC decoder and the compression modules which are identical to the AWGN case. Moreover, we note that the fully adaptive scheme depicted in Section IV-C for AWGN channel is also applicable to the fading scenario. The overall training

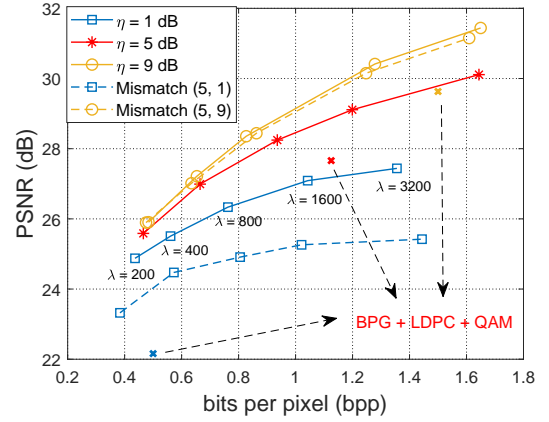


Fig. 9: Solid lines: R-D tradeoff for the proposed h-DJSCC framework. 15 different h-DJSCC models are trained and evaluated corresponding to $\eta \in \{1, 5, 9\}$ dB and $\lambda \in \{200, 400, 800, 1600, 3200\}$. Dashed lines: Models trained at $\eta = 5$ dB are evaluated under $\eta = \{1, 9\}$ dB.

procedure of the fully adaptive h-DJSCC framework for the Rayleigh fading channel is summarized in Algorithm 1.

V. NUMERICAL EXPERIMENTS

A. Parameter Settings and Training Details

Unless otherwise mentioned, the number of complex channel uses for the first hop is fixed to $k = 768$, which corresponds to $C_{out} = 24$. The number of channels, C_z and C_v , for z and v are set to 256 and 192, respectively.

Similar to the training setting in [7], we consider the transmission of images from the CIFAR-10 dataset, which consists of 50,000 training and 10,000 test images with 32×32 resolution. Adam optimizer is adopted with a varying learning rate, initialized to 10^{-4} and dropped by a factor of 0.8 if the validation loss does not improve in 10 consecutive epochs.

B. Performance Evaluation

1) *R-D performance for the proposed h-DJSCC framework:* Next, we focus on the proposed h-DJSCC framework and show that by training models with different λ values, the h-DJSCC framework can achieve different points on the R-D plane, enabling flexible adaptation to the user specific reconstruction requirement and latency constraint. Different $\eta \in \{1, 5, 9\}$ dB are evaluated and for each of the SNR value, we train different models with respect to different $\lambda \in \{200, 400, 800, 1600, 3200\}$ values.

The solid curves in Fig. 9 represent the PSNR performance versus bpp I defined in (12). For all η values, different bpp values are obtained with different models. When the latency constraint of the destination is stringent, we adopt a model with small λ , when the destination requires a better reconstruction performance, however, a large λ is preferable. We also find a better R-D curve is obtained when η is larger, which is intuitive as the first hop becomes less noisy.

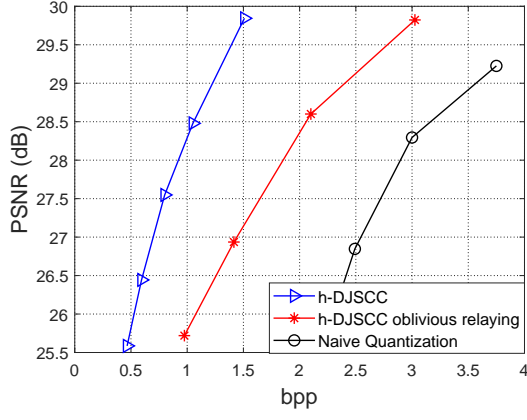


Fig. 10: Comparison of the R-D performance achieved by the h-DJSCC framework with/without oblivious relaying and the naive quantization scheme. In this simulation, we set $k = 768$, $\eta = 5$ dB.

The R-D performance of the fully digital and the naive quantization scheme is also evaluated. In particular, for the fully digital scheme, we consider BPG compression algorithm followed by LDPC code and QAM modulation with different code rates (e.g., $1/2, 3/4, 5/6$) and modulation orders (e.g., BPSK, 4QAM, 16QAM, 64QAM) for reliable transmission. For each η value, a specific code rate and modulation order which achieves the best R-D performance is adopted whose performance is shown in Fig. 9. As can be seen, for all η values, the proposed h-DJSCC framework achieves better R-D performance compared with the fully digital scheme. The performance of the naive quantization scheme is evaluated under $\eta = 5$ dB with $N_v = 2, b = 1$ whose PSNR equals to 18.8 dB and bpp equals to 1.5. Though naive quantization scheme is capable to avoid the cliff and leveling effects, its PSNR performance is outperformed by both the proposed h-DJSCC and the fully-digital baseline.

2) *Avoiding the cliff and leveling effects:* We then show that the proposed h-DJSCC framework is capable to avoid the cliff and leveling effects. In this simulation, models corresponding to different λ values trained at $\eta = 5$ dB are evaluated at $\eta = \{1, 9\}$ dB whose performances are represented by the dashed lines in Fig. 9. As shown in the figure, reasonable performance is maintained with mismatched SNR values which verifies the effectiveness of the proposed h-DJSCC framework.

3) *Oblivious relaying:* Finally, we provide simulation results of the oblivious relaying mentioned in Section III-B where the relay R_1 only has access to the past received signal \mathbf{y}_1 . We set $k = 768$, $\eta = 5$ dB and $\lambda = \{5, 7.5, 15, 25\}$ for this simulation. The relative performance of the oblivious relaying with the original h-DJSCC framework is shown in Fig. 10.

As expected, the R-D curve obtained from the oblivious relaying is worse than that of the original h-DJSCC framework. This can be understood from a goal-oriented [24] perspective as the neural compression and decompression modules, $f_c(\cdot)$ and $g_c(\cdot)$ of the h-DJSCC framework are jointly optimized for the final image reconstruction whereas $f_c^o(\cdot)$ and $g_c^o(\cdot)$ of the oblivious relaying model are trained to minimize the

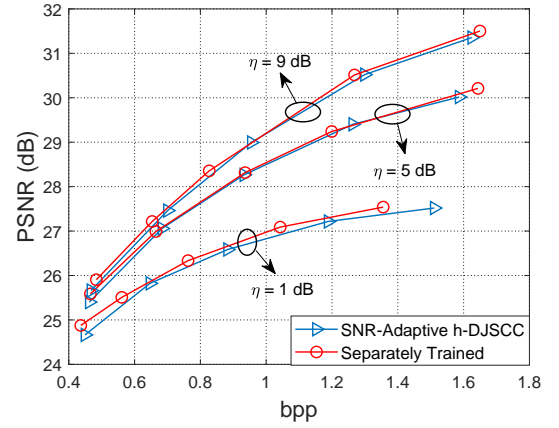


Fig. 11: Comparison of the R-D performance between the SNR-adaptive h-DJSCC models trained under varying $\eta \in [1, 9]$ dB values and the separately trained models.

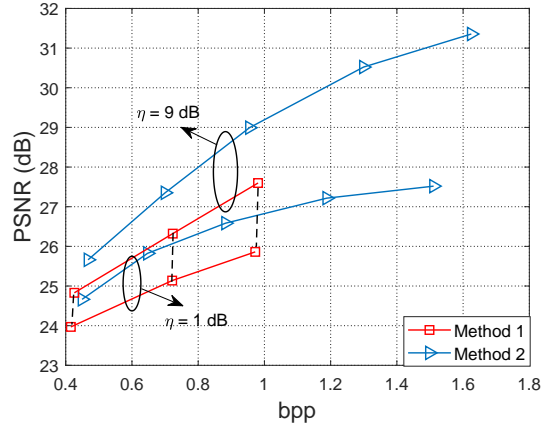


Fig. 12: R-D performance of the SNR-adaptive h-DJSCC model using different initialization methods. The dashed lines indicate nearly identical bpp values w.r.t different η values for the second method.

reconstruction error of the received signal \mathbf{y}_1 . Finally, we show the effectiveness of the proposed h-DJSCC framework under oblivious relaying protocol by comparing it with vector quantization baselines with $N_v = 2, b = \{1.5, 2, 2.5\}$ and $N_v = 3, b = 5/3$. As can be seen, the h-DJSCC scheme outperforms the naive quantization baseline by a bpp value greater than one.

C. Adaptive h-DJSCC Transmission

In this subsection, we will first show the R-D performance of the proposed SNR-adaptive h-DJSCC transmission. Then, we evaluate the proposed fully adaptive h-DJSCC framework.

1) *SNR-adaptive Transmission:* In this case, we consider a scenario with varying SNR values $\eta \in [1, 9]$ dB and train five different SNR-adaptive models corresponding to $\lambda \in \{200, 400, 800, 1600, 3200\}$. As illustrated in Section IV-B, we use the pre-trained SNR-adaptive DeepJSCC model to initialize $f_s(\cdot, \eta)$ and $g_d(\cdot, \eta)$ of the SNR-adaptive h-DJSCC model. Note that for the separately trained models, even if the

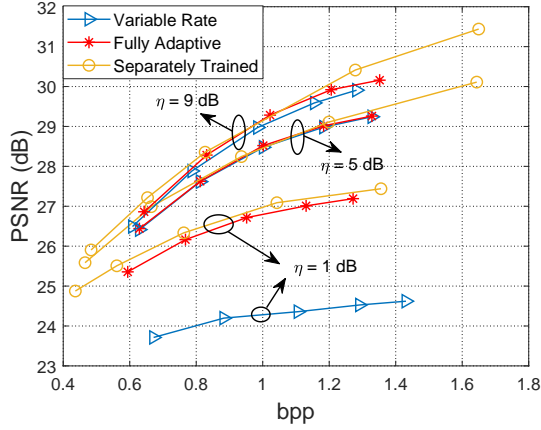


Fig. 13: Comparison of the R-D performance between the fully adaptive model, the separately trained models and the variable rate h-DJSCC model trained at a fixed η value.

SNR values are chosen with an interval equals to 4 dB, i.e., $\eta = \{1, 5, 9\}$ dB, we still need to train 15 different models.

The comparison of the R-D performance between the SNR-adaptive h-DJSCC models and the separately trained ones is shown in Fig. 11. For the SNR-adaptive h-DJSCC scheme, each R-D curve corresponds to a specific $\eta \in \{1, 5, 9\}$ value (with different λ values). As can be seen, the SNR-adaptive h-DJSCC models can achieve nearly the same R-D performance with the separately trained models which manifests the effectiveness of the proposed SNR-aware neural networks and the underlying probability models in Section IV-B.

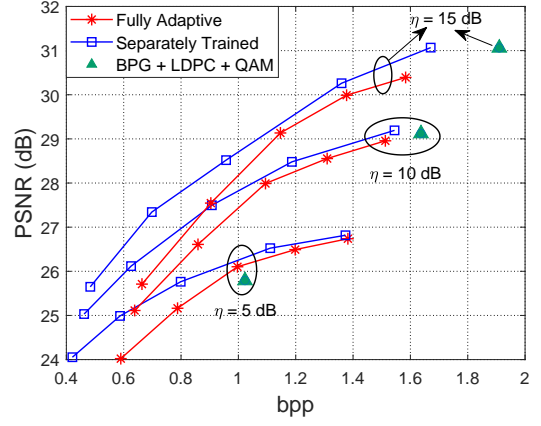
Then, we emphasize that the proposed initialization method is essential for satisfactory R-D performance. Two different initialization methods for the SNR-adaptive DeepJSCC encoder and decoder, i.e., $f_s(\cdot, \eta)$ and $g_d(\cdot, \eta)$, are evaluated. The first one (Method 1) adopts a random initialization while the second one (Method 2) loads the weights from the pre-trained SNR-adaptive DeepJSCC model and the weights are fixed during training⁹.

In this simulation, we train the SNR-adaptive h-DJSCC models corresponding to the two initialization methods under the same η range and λ values in Fig. 11. The relative performance of the two methods with $\eta = 1, 9$ dB is shown in Fig. 12. We can find the naive initialization method¹⁰ converges to sub-optimal solution whose R-D performance is significantly outperformed by the second method. It can also be seen that for a fixed λ , the bpp values of the random initialization method nearly keep the same w.r.t different η values which matches the analysis of the empirical distribution, $\hat{P}_{\tilde{x}_\eta}$ shown in Fig. 7. Thus, we adopt the second initialization method throughout this paper.

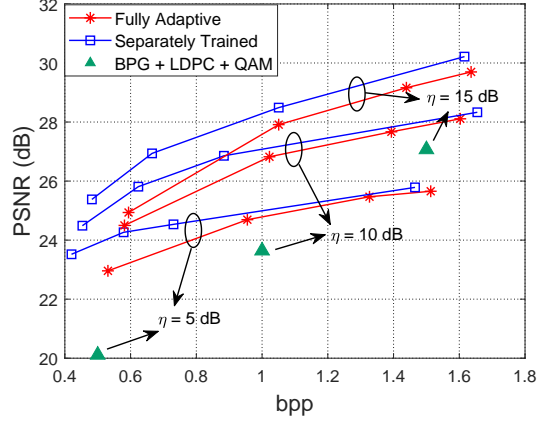
2) *Fully adaptive h-DJSCC framework*: Then, we evaluate the fully adaptive h-DJSCC framework whose aim is to use a single model to provide satisfactory R-D performance for each

⁹It is also possible to update/optimize the loaded weights during training, yet we find it leads to nearly the same performance compared with the fixed one.

¹⁰We show the results with $\lambda \in \{200, 1600, 3200\}$ for the random initialization method.



(a) CSI is available at both S and R_1 .



(b) CSI is only available at R_1 .

Fig. 14: Comparison of the R-D performance between the fully adaptive model, the separately trained models and the digital baseline over Rayleigh fading channel under two different setups.

and every combination of η and λ values. The model is trained with $\eta \in [1, 9]$ dB and $\lambda \in \{200, 400, 800, 1600, 3200\}$.

The R-D performance of the fully adaptive h-DJSCC framework is compared with the separately trained models under different λ and η values and a variable rate h-DJSCC model trained at a fixed $\eta = 5$ dB (with the same λ range). As shown in Fig. 13, we evaluate the three models under $\eta = \{1, 5, 9\}$ dB. Though outperformed by the separately trained models, the fully adaptive model still achieves satisfactory R-D performance for each combination of η and λ values. When compared to the variable rate h-DJSCC model trained at a fixed $\eta = 5$ dB, we find the fully adaptive h-DJSCC model outperforms it when evaluated under $\eta = \{1, 9\}$ dB and achieves similar performance when $\eta = 5$ dB. This aligns with the intuition that, since no SA module is adopted for the variable rate h-DJSCC model, its DeepJSCC encoder outputs the same codeword regardless of the mismatched channel conditions leading to sub-optimal R-D performance.

3) *Fading Channel*: To outline the effectiveness of the proposed h-DJSCC and the fully adaptive framework in the fading scenarios described in Section IV-D, we compare separately trained h-DJSCC models, the fully adaptive h-DJSCC model

with the digital baseline which utilizes BPG compression algorithm and delivers the compression output using a combination of different coded modulation schemes which is analogous to the setup in Fig. 9. For both fading scenarios with and without CSIT, the fully adaptive model adopts the second initialization method in Fig. 12 and is trained with $\eta \sim \mathcal{U}(5, 15)$ dB and $\lambda \in \{200, 400, 800, 1600, 3200\}$. The separately trained models are trained under a fixed $\eta \in \{5, 10, 15\}$ value and evaluated at the same SNR. We then briefly introduce the implementation of the digital baseline. For the fading scenario with CSIT, we select a coded modulation scheme which exhibits zero BLER for each η value and h implementation, the corresponding rate is denoted as $R_{\eta, h}$. The bit budget for the digital baseline is $kR_{\eta, h}$ and we adopt BPG compression algorithm to compress the image according to that budget. For the second scenario without CSIT, the transmitter has no access to h and a fixed coded modulation scheme is adopted for each η value. This leads to a non-zero BLER especially when the magnitude of h is small. The PSNR performance is obtained by averaging over the successful decoding cases and the failed ones.

The performance of the two fading scenarios with and without CSIT are shown in Fig. 14 (a) and (b), respectively. For both scenarios, the fully adaptive model can achieve comparable R-D performance with the separately trained models with large λ values, however, when λ is small, e.g., $\lambda = 200$, there is a bpp gap around 0.2. This aligns with the intuition that, it is hard to train a single model to be optimal for all the R-D points (λ values) simultaneously. We also observe that for both scenarios with and without CSIT, the proposed h-DJSCC schemes outperform the digital baseline as the R-D points obtained by the baseline scheme are strictly below the curves achieved by the proposed schemes. A larger gain over the baseline is observed for the fading scenario without CSIT, which is due to the fact that the performance of the baseline scheme drops significantly when it is incapable to select different coded modulation schemes according to different channel realizations, h . Note that our proposed schemes avoid the cliff and leveling effects in the meantime.

4) *Reduction in Storage:* It is worth mentioning the storage savings by adopting the fully adaptive h-DJSCC framework. As illustrated in Section III, the h-DJSCC framework can be divided into two parts, the DeepJSCC encoder ($f_s(\cdot)$) and decoder ($g_d(\cdot)$) as well as the compression ($f_c(\cdot)$) and decompression ($g_c(\cdot)$) modules. Denote the storage for $f_s(\cdot)$ and $g_d(\cdot)$ as T_1 while that for $f_c(\cdot)$ and $g_c(\cdot)$ as T_2 , then for different λ and η values, a total amount of $|\Lambda|H|(T_1 + T_2)$ space is required. The proposed fully adaptive h-DJSCC framework, on the other hand, only requires

$$T_1 + T_2 + \Delta T + 2c|\Lambda|(C_z + C_v) \quad (34)$$

amount of storage where ΔT denotes the additional cost to store the SA modules while c is a constant indicating the number of bytes to store each element of the scaling factors, $\{\mathbf{a}_\ell, \mathbf{a}'_\ell, \mathbf{b}_\ell, \mathbf{b}'_\ell\}, \ell \in [1, |\Lambda|]$. Since the additional terms are neglectable compared with T_1 and T_2 , the total required storage can be significantly reduced. In particular, we consider the

TABLE I: The comparison of the storage used by different schemes, namely, 1. separately trained models, 2. SNR-adaptive models and 3. fully adaptive model.

No.	1	2	3
Storage (Mb)	15*247.76	5*257.04	257.06

following setting where $\lambda \in \{200, 400, 800, 1600, 3200\}$ and $\eta = \{1, 5, 9\}$ dB. The required storage of the (1) separately trained models, (2) the SNR-adaptive models and (3) the fully adaptive model are shown in Table. I. As can be seen, the SA module and the scaling factors, $\{\mathbf{a}_\ell, \mathbf{a}'_\ell, \mathbf{b}_\ell, \mathbf{b}'_\ell\}, \ell \in [1, |\Lambda|]$ occupy merely 9.28 and 0.02 Mb, respectively yet adopting both of them is capable to reduce the overall storage cost by approximately $15\times$.

5) *Larger dataset:* Finally, we evaluate our scheme on the CelebA dataset [25] with a resolution equals to 128×128 to show the proposed h-DJSCC framework is effective for different datasets and is capable to provide visually pleasing reconstruction. In this simulation, the number of complex channel uses of the h-DJSCC framework in the first hop is set to $k = 3072$ and we consider an AWGN channel with $\eta = 5$ dB. This corresponds to a channel capacity equals to 2.05 which implies the maximum bit budget for the fully digital baseline is $\#b_s \approx 6298$. For the proposed h-DJSCC scheme, the same neural network architecture shown in Fig. 2 is adopted where the output channel of the DeepJSCC encoder is set to $C_{out} = 6$. The h-DJSCC model is trained with $\lambda = 1200$ leading to a bit budget smaller than that of the fully digital baseline, i.e., 6298. For the fully adaptive h-DJSCC model, we adopt the same training setting as in the CIFAR-10 setup where the model is trained with $\lambda \in \{200, 400, 800, 1600, 3200\}$ and $\eta \in [1, 9]$ dB while evaluated at $\lambda = 800$ and $\eta = 5$ dB.

The reconstructed images produced by our models are shown in Fig. 15 where we further provide a fully analog baseline adopting DeepJSCC-AF protocol illustrated in [1] which has three additional hops with identical channel qualities equal to 10 dB. As can be seen, the proposed h-DJSCC models outperform the fully digital baseline adopting BPG compression algorithm delivered at the AWGN channel capacity. It also outperforms the fully analog scheme which does not perform neural compression at R_1 . Moreover, it can be found that the fully adaptive h-DJSCC model achieves comparable performance with the separately trained one. Finally, compared with the fully digital baseline, the proposed h-DJSCC frameworks not only yield superior or equivalent PSNR and SSIM values but also produce visually pleasing reconstructions using less or equal amount of bits.

VI. CONCLUSION

This paper introduced a novel h-DJSCC framework tailored to enhance the reliability and efficiency of image transmission across hybrid wireless and wired multi-hop networks. Our study revealed that traditional approaches, which rely solely on fully digital transmissions, often fail to meet the demands of complex network architectures. To address these shortcomings,






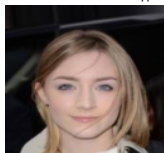
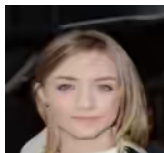
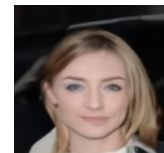
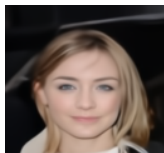


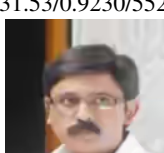
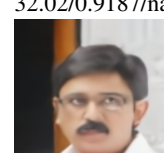
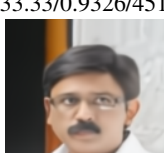
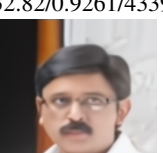
Ground Truth	Fully Digital	Fully Analog	Separately trained DJSCC	h- Fully adaptive h-DJSCC
 PSNR/SSIM/#b	 30.42/0.9280/6608	 31.70/0.9377/nan	 32.60/0.9467/4551	 32.27/0.9433/4029
 PSNR/SSIM/#b	 31.53/0.9230/5528	 32.02/0.9187/nan	 33.33/0.9326/4513	 32.82/0.9261/4339
 PSNR/SSIM/#b	 31.54/0.9231/5320	 32.20/0.9086/nan	 33.37/0.9215/4306	 32.93/0.9185/4176

Fig. 15: Visual comparison between the reconstructed images from CelebA dataset obtained from the proposed h-DJSCC frameworks, the fully analog scheme and the fully digital baseline with $\eta = 5$ dB and the number of complex channel uses in the first hop is set to $k = 3072$. The PSNR, SSIM and the number of bits (#b) to be transmitted over the remaining hops are provided.

we developed a hybrid solution that leverages DeepJSCC for the initial wireless hop to the access point, followed by a neural network-based compression model that effectively transforms the DeepJSCC codeword into a digital bitstream, suitable for stable transmission over subsequent wired hops to the edge server.

The implications of our work extend far beyond mere technical achievement. By providing a robust and adaptive solution that can effectively manage the complexities of transmitting high-quality images across hybrid multi-hop network conditions, we unlock new possibilities for real-world applications. From remote healthcare, where reliable and timely image transmission can be life-saving, to disaster response scenarios, where communication infrastructure is often compromised, our hybrid JSCC framework stands to revolutionize the way we handle data transmission in critical, bandwidth-sensitive environments.

REFERENCES

- [1] C. Bian, Y. Shao, and D. Gündüz, “A hybrid joint source-channel coding scheme for mobile multi-hop networks,” in *IEEE International Conference on Communications*, 2024.
- [2] E. Boursoulatzé, D. B. Kurka, and D. Gündüz, “Deep joint source-channel coding for wireless image transmission,” *IEEE Transactions on Cognitive Communications and Networking*, 2019.
- [3] P. Jiang, C.-K. Wen, S. Jin, and G. Y. Li, “Wireless semantic communications for video conferencing,” *IEEE J. Sel. Areas Commun.*, vol. 41, no. 1, pp. 230–244, 2023.
- [4] S. Wang, J. Dai, Z. Liang, K. Niu, Z. Si, C. Dong, X. Qin, and P. Zhang, “Wireless deep video semantic transmission,” *IEEE J. Sel. Areas Commun.*, vol. 41, no. 1, pp. 214–229, 2023.
- [5] H. Xie, Z. Qin, G. Y. Li, and B.-H. Juang, “Deep learning enabled semantic communication systems,” *IEEE Transactions on Signal Processing*, vol. 69, pp. 2663–2675, 2021.
- [6] C. Bian, Y. Shao, and D. Gündüz, “Wireless point cloud transmission,” *arXiv preprint arXiv:2306.08730*, 2023.
- [7] C. Bian, Y. Shao, H. Wu, E. Ozfatura, and D. Gündüz, “Process-and-forward: Deep joint source-channel coding over cooperative relay networks,” *arXiv:2403.10613*, 2024.
- [8] B. Tang, L. Huang, Q. Li, A. Pandharipande, and X. Ge, “Cooperative semantic communication with on-demand semantic forwarding,” *IEEE Open Journal of the Comms. Soc.*, vol. 5, pp. 349–363, 2024.
- [9] W. An, Z. Bao, H. Liang, C. Dong, and X. Xu, “A relay system for semantic image transmission based on shared feature extraction and hyperprior entropy compression,” *IEEE Internet of Things Journal*, pp. 1–1, 2024.
- [10] S. F. Yilmaz, C. Karamanli, and D. Gündüz, “Distributed deep joint source-channel coding over a multiple access channel,” in *IEEE International Conference on Communications*, 2023.
- [11] T. Wu, Z. Chen, M. Tao, B. Xia, and W. Zhang, “Fusion-based multi-user semantic communications for wireless image transmission over degraded broadcast channels,” *arXiv:2305.09165*.
- [12] Y. Yin, L. Huang, Q. Li, B. Tang, A. Pandharipande, and X. Ge, “Semantic communication on multi-hop concatenated relay networks,” in *2023 IEEE/CIC International Conference on Communications in China (ICCC)*, 2023, pp. 1–6.
- [13] G. Zhang, Q. Hu, Y. Cai, and G. Yu, “Alleviating distortion accumulation in multi-hop semantic communication,” *IEEE Communications Letters*, vol. 28, no. 2, pp. 308–312, 2024.
- [14] Y. Shao and D. Gündüz, “Semantic communications with discrete-time analog transmission: A PAPR perspective,” *IEEE Wireless Communications Letters*, vol. 12, no. 3, pp. 510–514, 2022.
- [15] D. Samardzija, J. Pastalan, M. MacDonald, S. Walker, and R. Valenzuela, “Compressed transport of baseband signals in radio access networks,” *IEEE Transactions on Wireless Communications*, vol. 11, no. 9, pp. 3216–3225, 2012.
- [16] H. Si, B.-L. Ng, M.-S. Rahman, and J. Zhang, “A novel and efficient vector quantization based CPRI compression algorithm,” *IEEE Transactions on Vehicular Technology*, vol. 66, no. 8, pp. 7061–7071, 2017.
- [17] J. Ballé, D. Minnen, S. Singh, S. J. Hwang, and N. Johnston, “Variational image compression with a scale hyperprior,” in *International Conference on Learning Representations*, 2018.
- [18] I. E. Aguerri, A. Zaidi, G. Caire, and S. S. Shitz, “On the capacity of cloud radio access networks with oblivious relaying,” *IEEE Transactions on Information Theory*, vol. 65, no. 7, pp. 4575–4596, 2019.
- [19] A. Homri, M. Peleg, and S. S. Shitz, “Oblivious fronthaul-constrained relay for a gaussian channel,” *IEEE Transactions on Communications*, vol. 66, no. 11, pp. 5112–5123, 2018.
- [20] J. Xu, B. Ai, W. Chen, A. Yang, P. Sun, and M. Rodrigues, “Wireless

- image transmission using deep source channel coding with attention modules,” *IEEE Trans. on Circuits and Systems for Video Tech.*, 2021.
- [21] T. Chen and Z. Ma, “Variable bitrate image compression with quality scaling factors,” in *2020 IEEE International Conference on Acoustics, Speech and Signal Processing (ICASSP)*, 2020, pp. 2163–2167.
 - [22] Z. Cui, J. Wang, S. Gao, T. Guo, Y. Feng, and B. Bai, “Asymmetric gained deep image compression with continuous rate adaptation,” in *Proceedings of the IEEE/CVF Conference on Computer Vision and Pattern Recognition*, 2021, pp. 10532–10541.
 - [23] F. Yang, L. Herranz, J. v. d. Weijer, J. A. I. Guitián, A. M. López, and M. G. Mozerov, “Variable rate deep image compression with modulated autoencoder,” *IEEE Signal Processing Letters*, vol. 27, pp. 331–335, 2020.
 - [24] P. A. Stavrou and M. Kountouris, “A rate distortion approach to goal-oriented communication,” in *2022 IEEE International Symposium on Information Theory (ISIT)*, 2022, pp. 590–595.
 - [25] Z. Liu, P. Luo, X. Wang, and X. Tang, “Deep learning face attributes in the wild,” in *Proceedings of International Conference on Computer Vision (ICCV)*, December 2015.